Journal Pre-proof

White Etching Structures in Annealed 52100 Bearing Steel Arising from High-Pressure Torsion Tests

L.V. Wilches Pena, L. Wang, B.G. Mellor, Y. Huang

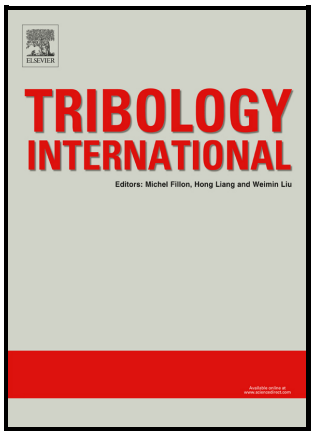

PII: S0301-679X(21)00335-2

DOI: https://doi.org/10.1016/j.triboint.2021.107187

Reference: JTRI107187

To appear in: *Tribiology International*

Received date: 29 March 2021
Revised date: 6 July 2021
Accepted date: 11 July 2021

Please cite this article as: L.V. Wilches Pena, L. Wang, B.G. Mellor and Y. Huang, White Etching Structures in Annealed 52100 Bearing Steel Arising from High-Pressure Torsion Tests, *Tribiology International,* (2021) doi:https://doi.org/10.1016/j.triboint.2021.107187

White Etching Structures in Annealed 52100 Bearing Steel Arising from High-Pressure Torsion Tests.

L. V. Wilches Pena [a, (1)], L. Wang [a], B. G. Mellor [a], Y. Huang [a, b]

[a] national Centre for Advanced Tribology at Southampton (nCATS), Faculty of Engineering and the Physical Sciences, University of Southampton, Southampton, Hampshire, England, UK - SO17 1BJ. ling.wang@soton.ac.uk, B.G.Mellor@soton.ac.uk

[b] Department of Design and Engineering, Faculty of Science and Technology, Bournemouth University, Poole, Dorset, England, UK - BH12 5BB. yhuang2@bournemouth.ac.uk

Abstract.

White Etching Areas observed in failed rolling bearings have been associated with the presence of Severe Plastic Deformation conditions, which can be achieved by High-Pressure Torsion tests; thus, this technique was selected to produce White Etching Structures in annealed AISI 52100. Their origin arises from two main phenomena: Firstly, the relative movement between anvil/samples creates instabilities and interruption to plastic flow close to the surface of the sample. Secondly, the presence of hard discontinuities such as carbide clusters and non-metallic inclusions interrupt plastic flow

(1) Corresponding author details:

Current address:

Universidad EIA, Escuela de Ingeniería y Ciencias Básicas, Grupo MAPA.

Km 2 + 200 Variante Aeropuerto JMC

Envigado, Antioquia, Colombia

Email:

luis.wilches@eia.edu.co

inside the samples. Both phenomena seem to promote carbide dissolution in the ferritic matrix and so could produce not only White Structures but also White Etching Areas.

Keywords.

White Etching Areas, AISI 52100, High-Pressure Torsion.

1. Introduction.

Over recent years, White Etching Areas (WEAs) in bearing steels have received increasing attention due to their relationship with premature failures of rolling element bearings, especially those assembled in wind turbine gearboxes. WEAs have been linked to a catastrophic surface damage phenomenon commonly called Brittle Flaking Wear (BFW) [1] or White Structure Flaking (WSF) [2] [3] that appears visible to the naked eye as smearing, cracks, and macro pitting. Although spalling resulting from Rolling Contact Fatigue (RCF) would normally be expected to limit bearing service life to 20 years based on the L_{10} life estimate, WEAs formation and WSF can reduce this to as short as 5 - 10% of the L_{10} bearing life [4]. WEAs are a particular type of microstructure in steels, which appears to be white under Light Optical Microscopy (LOM) after etching. The white appearance is due to their higher corrosion resistance to Nital etch compared to the matrix that surrounds them [4]. WEAs have been related to microstructural discontinuities such as non-metallic inclusions [5-7], carbide clusters [8, 9] and cracks [10-12]. These discontinuities could interact with the Hertzian stresses in the subsurface of the contact areas to generate localized and Severe Plastic Deformation (SPD) conditions. SPD could promote grain refinement and dissolution of carbides in well-defined regions. Both phenomena seem to be closely related to WEAs initiation and evolution [13-19]. Similar mechanisms have been suggested to explain the origin of some white microstructures encountered in pearlitic steels processed by High-Pressure Torsion tests (HPT) [20]. HPT has also been used recently to study the mechanical decomposition of cementite by SPD in a quenched/tempered AISI 52100 bearing steel and its role in the formation of WEAs [21] and to understand the nature and formation mechanism of White Etching Layers (WELs) in rail track steels [22]. HPT, as an SPD process, is generally conducted on a thin disc sample placed between two anvils that transmit compression and high torsional stresses through the rotation of one of the anvils. The combination of compression and

shear stresses can produce homogeneous microstructures with grain sizes of less than 1 μm [23].

Although HPT differs from RCF in many ways, it provides a fast procedure and simplifies the microstructure alteration formation to the influence of stresses only and eliminates the influence of lubricants, heat, electricity etc. but focuses on the effect of shear and compressive stress. Moreover, HPT tests are simple to perform and allow easy repeatability compared to both RCF tests and the analysis of field bearings, which usually require millions of cycles to produce WEAs [24, 25], whilst HPT requires just a few minutes to process one disc. Parameters such as pressure, strain (measured as rotational displacement or turns), rotational speed and temperature can be easily controlled, allowing efficient sample processing under different conditions. However, important limitations are associated with HPT tests. One of these limitations is that the admissible final hardness of discs must be lower than the anvil hardness to avoid permanent damage to the anvils and the HPT test machine. Hence the original bearing roller samples were annealed to enable them to be HPT processed. This has enabled the study the microstructural changes produced under the influence of compressive and torsional stresses.

This paper presents the microstructural variations found after HPT tests conducted on annealed AISI 52100 bearing steel, using pressures and turns limited by the hardness limits admissible for the HPT testing machine. The most important result observed after carrying out HPT tests was the formation of White Etching Structures (WES) in different regions. Hence, this paper focuses on WES characterisation via LOM and Scanning Electron Microscopy (SEM). As WES and WEAs share significant similarities, the information obtained from WES could help shed light on the initiation and evolution of WEAs in a bearing steel affected by SPD conditions.

2. Methodology.

2.1 Material preparation.

The material selected was an AISI 52100 bearing steel provided by a local supplier (Simply Bearing Ltd. Halton House, Greenfold Way, Leigh WN7 3XJ, UK) as standard rollers 10 mm in diameter and 14 mm long with 750 ± 10 HV hardness. As the HPT test

machine available only allows the final hardness of the sample to be 800 HV, an annealing heat treatment as detailed in [26] was conducted on the AISI 52100 rollers to reduce the hardness of the rollers to 180 ± 10 HV prior to the HPT tests. After this heat treatment, the roller diameter was observed to have reduced to 9.8 mm after eliminating the decarburised layer on the roller surface produced during annealing. The rollers were then cut into 1 mm thick slices followed by grinding using 800 and 1200 grade silicon carbide paper to obtain a final disc thickness of 0.8 – 0.9 mm. Detailed technical information on AISI 52100 standard rollers can be found in reference [27].

2.2 HPT tests.

HPT tests were conducted on the thin disc samples using an HPT machine manufactured by Riken Enterprise Co. Ltd. in Kokuraminami Ku Kitakyusyu City (Japan) under 0.5, 1, 3, 6 GPa pressure calculated as applied load over the cross-section area of the disc samples. However, recent FEM and experimental work has shown that the hydrostatic pressure is not uniform over the disc surface; it decreases with increasing distance from the disc centre, remains unchanged across the disc thickness and the pressure at the centre is higher than that calculated on load over cross-sectional area [28]. Both experiments and simulations indicate that the mean hydrostatic pressure during HPT processing closely corresponds to the compressive load over the disc area plus the contact area between the anvils, thus that mean pressure calculated on just the cross-section area overestimated the mean pressure by a factor of 2 [28]. Tests were restricted to 1, 2, 3 turns were used under these pressures to avoid damaging the anvils by the significant hardness increases observed during the HPT test. At least two repeat tests were conducted for each condition. All tests were conducted at ambient temperature without lubrication at a rotational speed of 1 rpm of the lower anvil, the upper anvil being stationary. Because of the large amount of information available on HPT tests conducted on steels using 1, 2, 3 turns under 1 rpm, the number of turns and the rotational speed were chosen so as to provide useful comparative results to other HPT studies on steels [20] [29-37]. The rotational speed was measured manually using an external chronometer. All tests were conducted rotating in an anticlockwise sense with respect to the top anvil. These parameters were also chosen to protect the HPT anvil integrity due to the significant hardness increment found in the samples after 3 turns.

An adhesive tape was used to collect carefully the debris remaining on the surface of the cavity in the upper anvil which had been in contact with the sample. In this way debris resulting from flash formation during HPT was not collected. To determine if slippage had occurred during the HPT tests (up to 1 turn), the method developed by Edalati et. al. [38] has been used, where two parallel lines were drawn across the diameter of both top and bottom surfaces of the discs prior to the HPT testing. The angular displacement of the two lines was then measured in degrees and compared with the angular rotational of the machine after HPT testing. Any difference in angular displacement of the lines and the machine rotation angle allows the slippage between the anvil and sample surface to be determined. All flash produced at the edge of the samples during the HPT tests was removed by grinding followed by detailed metallography of the disc.

2.3 Characterisation of the HPT processed samples.

Features of the HPT processed samples have been characterised by standard metallography and etching techniques. HPT samples were mounted in Bakelite, ground to 4000 grade SiC paper and polished using suspensions of 6 µm / 1 µm diamond pastes using a Struers TegraPol 15 machine. Grinding was carried out with 10 - 15 N pressure while the polishing pressure was 25 N. Etching with 2% Nital (2ml HNO_3, 98ml ethanol) was conducted to reveal carbide distribution and WES. The HPT tested samples were analysed in three ways: Firstly, 40 µm was ground and polished from both their top and bottom surfaces to study differences in the roughness patterns of the two surfaces in each sample as well as between all tested samples. Then, selected samples were ground and polished 360 µm in successive steps from the bottom surface to find subsurface WES. Some disc samples were also cut along their diameters in the axial direction to reveal WES both on the surface and subsurface. All these sections were firstly subjected to a preliminary inspection by LOM after etching to identify any microstructural variations. Following this detailed analysis by LOM and SEM, (JEOL JSM-6500F with SEI/BSI detectors and FEI/Philips XL30 ESEM with SE/BSI/GSI detectors) was carried out to characterise the size and morphology of the WES.

An Image Processing Program (IPP) *Image J – Flavour Fiji* was used to quantify the WES formed on the top surface. The *Threshold* tool was utilised to generate black/white masks

from the LOM images and to visualize the WES; the *Particle Analysis* tool was then used to exclude unwanted objects as a function of their sizes (20, 40 and 60 μm^2*)*. This led to the WES appearing as black patches whilst the matrix appeared white. Finally, the black percentage in the images was obtained using the tool *Analyze* / *Measure* [39]. Thus, to study the WES located at the top surfaces as a function of the pressure and number of turns, four representative LOM images were taken every 90° around the circumferential direction centred at a radial distance of 3.5 mm, Figure 1 a). The % of black masks generated by *Image J* was calculated for all images, thus obtaining 4 measurements of the % WES per sample. This procedure was repeated twice and hence 8 measurements of the % WES were acquired from the two samples. Finally, an average of all 8 values was reported as a representative % WES for each HPT parameter combination (pressure and turns). Figure 1 a) shows a schematic of the positions of the four selected areas on a disc surface, whilst Figure 1 b) and c) show examples of one image analysed and its corresponding black / white mask.

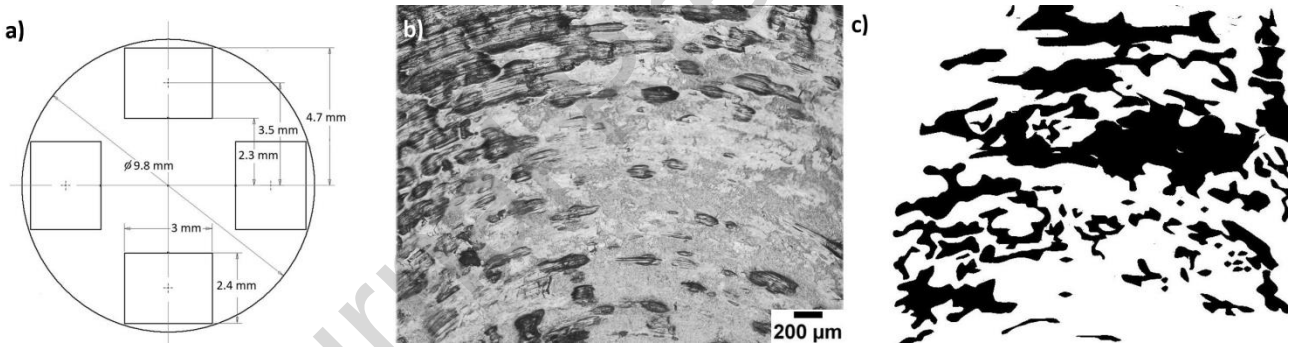

Figure 1. Quantification of % WES on the top surface of the sample discs processed by HPT. a) Position of the representative areas analysed by IPP (measurements in mm). b) Micrograph taken at a radial distance of 3.5 mm from the centre. c) IPP *Image J* used to determine the % WES to the area showed in b).

2.4 Micro and nano hardness measurements.

To evaluate the hardness of WES in relation to its surrounding matrix, micro and nano hardness measurements were taken. A Matzusawa Seijki MHT-1 micro hardness tester with a Vickers indenter (100 g load for 15 s) and a NanoTest, Vantage Micro Materials Ltd, with a Berkovich indenter (0.05 mN initial load and indenter contact velocity of 0.5 μm/s)

were used. Micro hardness values were taken on the WES and in areas adjacent using the edge of the sample as a geometrical reference. However, their position was then defined with respect to the centre of the sample using an Olympus BX51 LOM and the IPP Image J.

In addition, nano hardness maps were constructed from measurements taken in a region affected by WES located on the top surface located on a circumferential section). Nano-hardness tests were carried out using a *Depth Controlled Mode* with a setup of 200 nm maximum depth, to avoid any penetration of the ferritic matrix beneath the WES. The selection of nano indentation parameters was based on previous experience measuring other metals with similar or higher hardness than that expected for the deformed AISI 52100. A grid of 10 x 10 indentations separated by 5 μm was used. The separation between indentations was the minimum admissible to avoid plastic effects between neighbouring indents. The NanoTest Analysis Mode software was used to process the data and produce the maps.

2.5 Anvil roughness measurements.

The anvil assembly was of a quasi-constrained configuration with a cavity 10 mm in diameter and 0.25 mm deep in both top and bottom anvils. The cavity vertical walls have a 22^0 chamfer to facilitate plastic flow. The cavity allows sample discs of 9.8 mm diameter and 0.8-0.9 mm thickness to be processed. The width of the contact area between the two anvils, where the flashes is formed, is 2 mm. To obtain an impression of the roughness of the anvils some sample discs were compressed by the HPT test machine under pressures of 1, 3 and 6 GPa. The impressions on both top and bottom sides of the disc samples were evaluated using a Taylor Hobson Form Talysurf 120L profilometer system to obtain roughness profiles along the diameter of the disc samples. The lengths selected to be measured were taken along five random diameters of each sample studied (unprocessed, compressed under 1, 3 and 6 GPa). The main results of these measurements are reported in Table 2. In addition, a reconstruction of the surfaces was made using an Alicona G4 Infinite Focus optical system (Figure 12). To evaluate the Ra, Rq, Rz parameters from the surfaces, the standard recommendations in BS EN ISO 4288-1998 were followed [40]. The cut – off (λc) selection depended on the spacing of the profile features, peaks, and valleys

(RSm), which was estimated through visual inspection. For the HPT samples, two RSm values were selected 0.13-0.4 mm for the unprocessed samples and 0.4 -1.3 mm for the deformed ones.

3. Results.

3.1 Annealed microstructure.

The microstructure of the annealed AISI 52100 consisted of a ferritic matrix with an approximately homogeneous distribution of spheroidal carbides of different shapes and size. Etching with 2% Nital was effective at revealing the carbides but did not reveal all the ferritic grain boundaries (Figure 2 a)). Although the main part of these carbides looked “spheroidal”, a few of them appeared as pearlitic lamellae structures in very well-defined areas. (White arrows in Figure 2 b)).

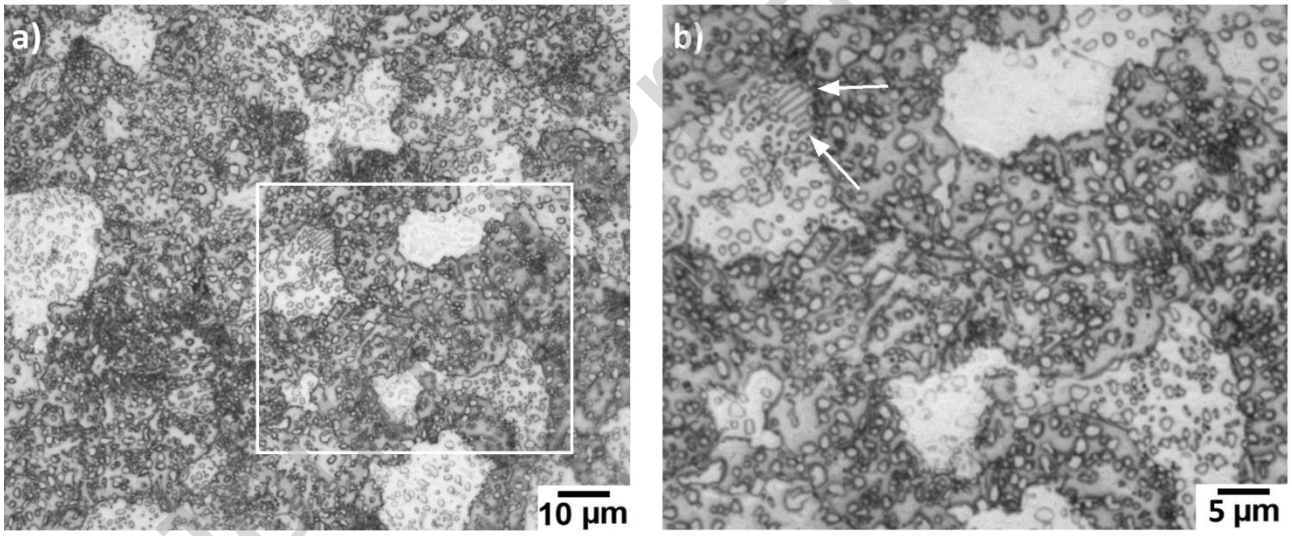

Figure 2. Microstructure of an axial section of an annealed AISI 52100 rollers. The white rectangle shows a region detailed in b). a) Not all ferritic boundary grains were visible by LOM after etching. b) Lamellae from the pearlitic structures still present after the annealing heat treatment. LOM Nital 2%.

3.2 Evidence of slippage.

Macroscopic examination of the HPT tested samples revealed that slippage between the top anvil and the disc top surface has occurred during the testing. By inspecting the lines

drawn along sample diameters prior to and after testing, the amount of slippage in degrees after 1 turn was calculated. The percentage slippage was also calculated in relation to the 360-degree corresponding to one turn of the machine. It was not possible to assess the slippage after more than one turn as the drawn lines were then no longer visible after HPT testing. Table 1 gives the slippage measured after HPT for 1 turn. Five measurements were taken for each test configuration.

Table 1. Slippage in HPT tests after 1 turn. The values correspond to averages from 5 samples.

HPT parameters	**Slippage angle (^{o})**	**% Slippage**
1 GPa 1 T	80.2 ± 2.2	22.3
3 GPa 1 T	52.6 ± 1.9	14.6
6 GPa 1 T	29.6 ± 1.7	4.05

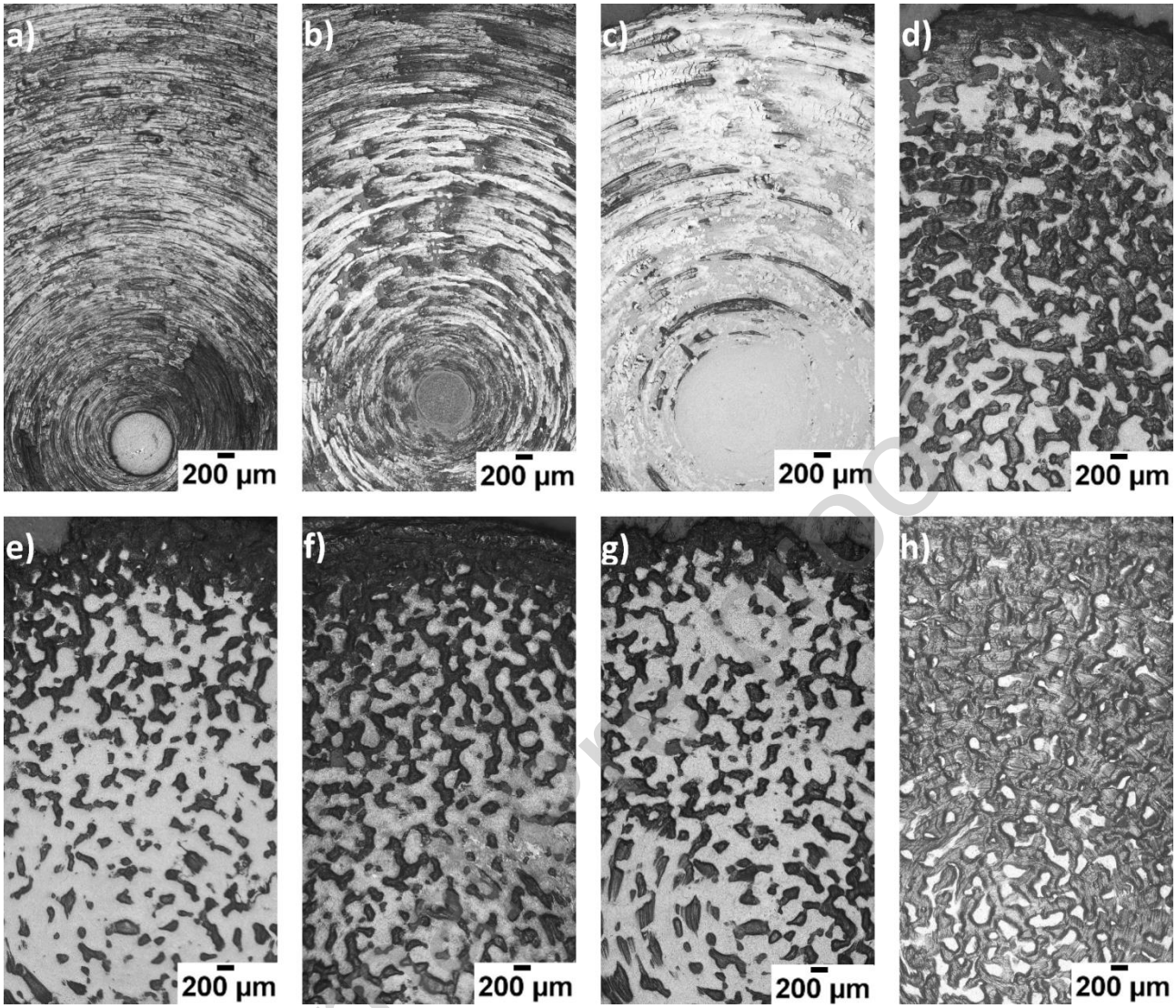

Figure 3. Montages of top (Images from a) to d)) and bottom (Images from e) to h)) surfaces of annealed AISI 52100 samples after conducting HPT tests using 0.5, 1 GPa, 3 GPa, 6 GPa and 1 turn. The top surface exhibited grooves alternated by white patches; the bottom surface showed an *orange peel* pattern. LOM, Nital 2 %.

3.3 Differences between top and bottom surfaces.

The top and bottom surfaces of the discs had a different appearance: concentric circle tracks alternated by smooth and shiny regions appeared on the top surface (Figure 3, images a) to c)), whilst a pattern similar to an *orange peel* appeared on the bottom surface (Figure 3, images e) to h)). When the pressure applied was 6 GPa, this *orange peel* pattern also appeared on the top surface of the disc samples (Figure 3, image d)). A thin

extruded ribbon or flash was observed to form concentrically around the middle periphery of the disc for all samples processed, the size of this flash increasing with higher pressure and number of turns.

All samples remained adhered to the bottom anvil once the HPT tests ended. The circular tracks shown in the upper images of Figure 3 (for tests carried out at 0.5, 1 and 3 GPa), appeared as discontinuous grooves alternated by shiny and smooth patches that looked white after etching. These white patches covered the main part of the top surfaces as a succession of concentric rings, except for a small circular area at the centre of the samples; their extent and shape seemed to be related to the pressure applied during the HPT tests. For pressures of 0.5 to 1 GPa, they looked slim and elongated and affected large areas, whilst at 3 GPa their incidences were less despite their bigger size. The lower images in Figure 3 shows the *orange peel* pattern which affected the bottom side of all samples processed by HPT tests. On samples processed using 6 GPa, this pattern covered the top surface as well, replacing the grooves and white patches.

3.4 WES on the top surface and in the subsurface.

A detailed microstructural characterisation via LOM revealed several changes in the annealed microstructure after HPT tests. These changes included evidence of plastic deformation, carbide redistribution and WES, which were found in two different regions: close to the top surface (designated as Top White Etching Areas or TWES) and in the subsurface of the samples, 240-360 µm from the bottom side, (designated as Subsurface White Etching Areas or SWES). TWES were observed after grinding 40 µm from the top surface of the discs (in contact with the stationary anvil) to remove the roughness or grooves caused by slippage between the top surface and the anvil whilst SWES were explored by serial sectioning from the bottom side at 40 µm intervals. Both TWES and SWES were also studied on axial sections cut along the diameter of the samples.

3.4.1 TWES (at the top surface).

LOM revealed a large number of TWES at radial distances of between 1.5 mm and 5 mm on all samples except those processed under 6 GPa. Figure 4 a) shows a LOM image of the TWES from the sample processed using 1 GPa 1 turn. Details of the region b are also

shown in Figure 4 b). TWES appeared elongated and in irregular patches that seemed to follow the circular tracks on the sample. In some cases, TWES alternated with grooves, in other cases they overlapped them. Regions of higher plastic deformation were visible where patches overlapped each other more, producing bigger TWES (Figure 4 a), area enclosed by yellow line); In other places, small isolated TWES appeared, but their orientation and shape suggested that they were part of larger TWES located at the same radial position (Figure 4 a) white arrows). Both linked and isolated TWES seem to be related to the high plastic deformation imposed by the rotation of the sample against the upper anvil. A fibrous structure was visible inside some TWES, the fibres extended along TWES forming a swirl or vortex pattern in some regions (Figure 4 b), areas enclosed by yellow lines). Some cracks were also observed following the fibres, especially close to the TWES borders, others crossed TWES in a radial direction (Figure 4 b), white arrows). The matrix that surrounded the TWES and grooves appeared as a continuous ferrite phase with many small spheroidal carbides, approximately 2 µm diameter that seem to be distributed relatively uniformly at first sight. No carbides were observed inside the TWES by LOM. Features found in this sample have also been found in other samples.

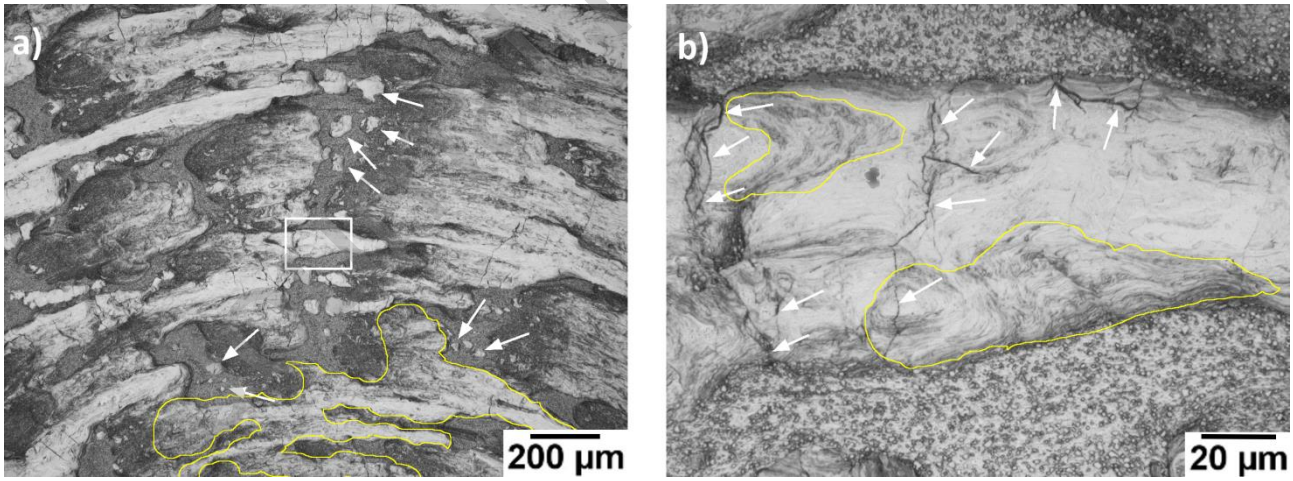

Figure 4. Details of WES structure on the top surface of a sample processed with HPT. a) Overlapping TWES in a circular pattern at 3.5 mm radial distance (area enclosed by yellow line) and isolated TWES that seemed to be part of a bigger TWES (white arrows). The white rectangle shows the region detailed in b). b) The fibrous structures inside the TWES adopt a swirled morphology (areas inside yellow lines); note the crack morphology present in the TWES (white arrows). 1 GPa 1 turn, LOM, Nital 2 %.

SEM / SEI images taken of the smooth and shiny regions revealed that TWES consisted of several overlapped layers affected by high plastic deformation of the ferritic matrix. The overlapping phenomenon seemed to be caused by the sliding contact between the disc sample and the anvil, which deformed plastically the ferritic matrix and the TWES. This phenomenon is visible in Figure 5 a), where some TWES located at a radial distance of 3.5 mm on the top surface of a sample processed using 0.5 GPa 1 turn are shown. The smooth surface of the TWES appears to be comprised of several overlapped layers stacked over each other as a result of plastic deformation. Flakes were visible on TWES at several radial distances but were present in greater amounts when the pressure and the number of turns were higher. They were formed by the high plastic deformation resulting from sliding which generated severe adhesive wear conditions. Figure 5 b) shows some of these flakes on a TWES located at a radial distance of 3.5 mm in a sample processed by 1 GPa 1 turn.

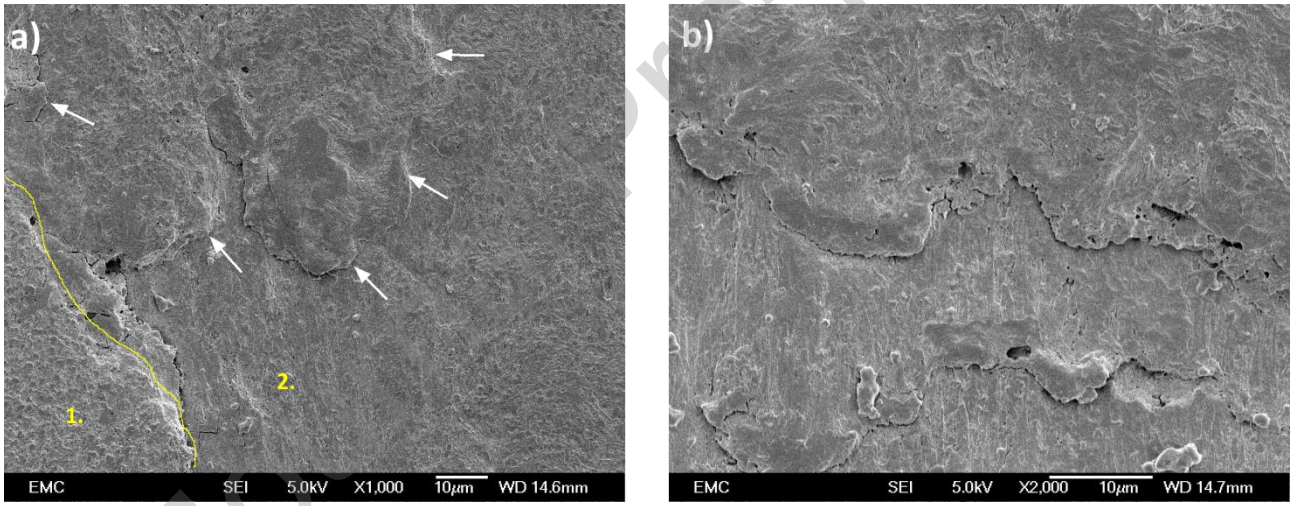

Figure 5. a) Differences between the appearance of the deformed ferritic matrix (1) and TWES (2). TWES layers appeared to overlap (white arrows) b) Flakes on TWES produced by severe sliding and high plastic deformation. 0.5 GPa 1 turn, SEM/SEI Nital 2 %.

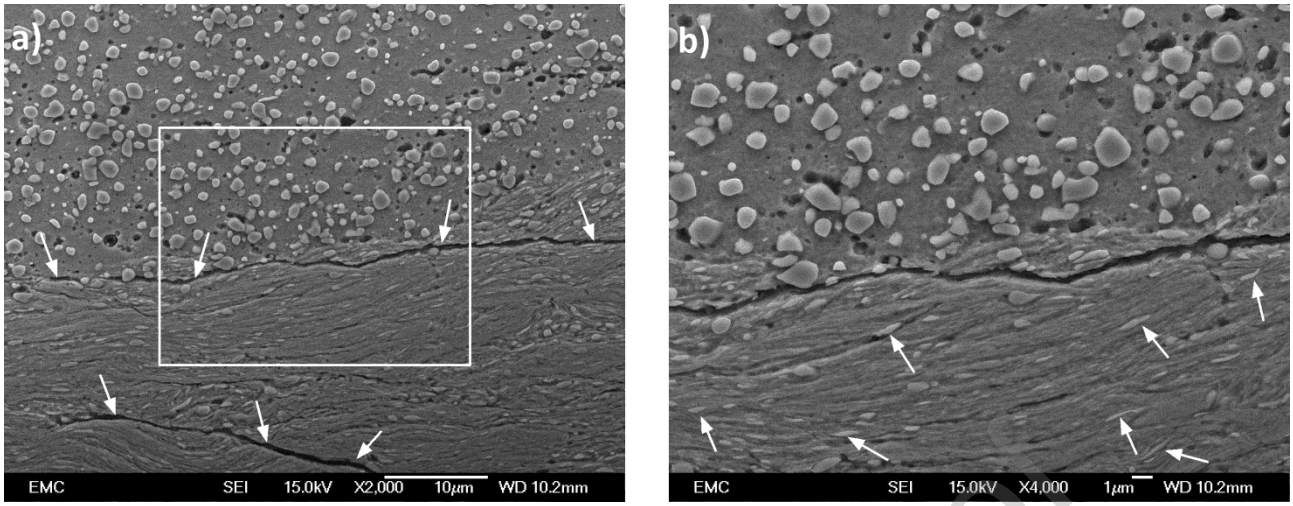

Figure 6. Details on an axial section of a sample processed using 1 GPa and 2 turns. The white rectangle indicates the area shown at higher magnification in b). a) Differences between the carbide distribution located in the deformed ferritic matrix and the TWES. Some small cracks are visible inside of TWES and near to the deformed ferritic matrix (white arrows). b) Deformed carbides linked to the fibrous structure in a cloud TWES (white arrows). The top surface of the sample is located at the bottom of these images. SEM/SEI Nital 2 %.

A detailed SEM /SEI analysis conducted on axial sections revealed other interesting features of the TWES. Firstly, TWES is clearly different from the deformed ferritic matrix due to its fibrous microstructure. Small crack systems were observed along TWES, but especially near to the deformed ferritic matrix (white arrows in Figure 6 a) and separating both phases in several cases. Fewer carbides were observed inside the TWES, and their distribution between the fibres was non-uniform, compared to their relatively homogeneous distribution in the matrix. Moreover, carbides in the TWES were smaller, deformed, and in some cases appeared linked to the TWES fibres (white arrows in Figure 6 b)). A similar behaviour has been reported previously in annealed AISI 52100 sample discs processed with HPT [41].

Eventually, with higher pressures and number of turns, cracks form inside or below these flakes which promote material detachment. A dramatic reduction in the areas affected by TWES was noted on a more highly deformed surface, i.e. on samples processed using 3 GPa and 3 turns. Abrasion and adhesion combined appear to have removed the majority

of the TWES, leaving just a few TWES clusters oriented in the sliding direction. The abrasion and adhesion eventually produced wear debris that was trapped between the contacting surfaces. Wear debris collected from the cavity in the upper anvil after conducting a HPT test using 3 GPa 3 turns is shown in Figure 7.

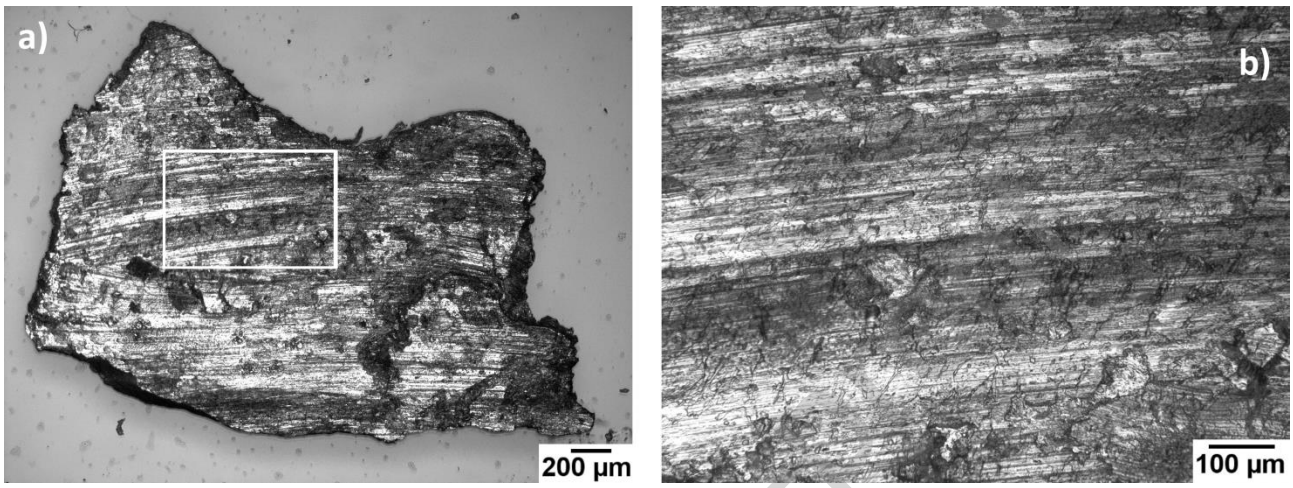

Figure 7. Debris collected from the cavity of the upper anvil after conducting a HPT test. The white rectangle indicates the area shown at higher magnification in b). a) Optical image of debris produced after processing a sample disc under 3 GPa 3 turns. b) Detail of debris surface exhibiting typical sliding wear features, such as high plastic deformation, delamination and grooves produced by abrasion. LOM Nital 2 %.

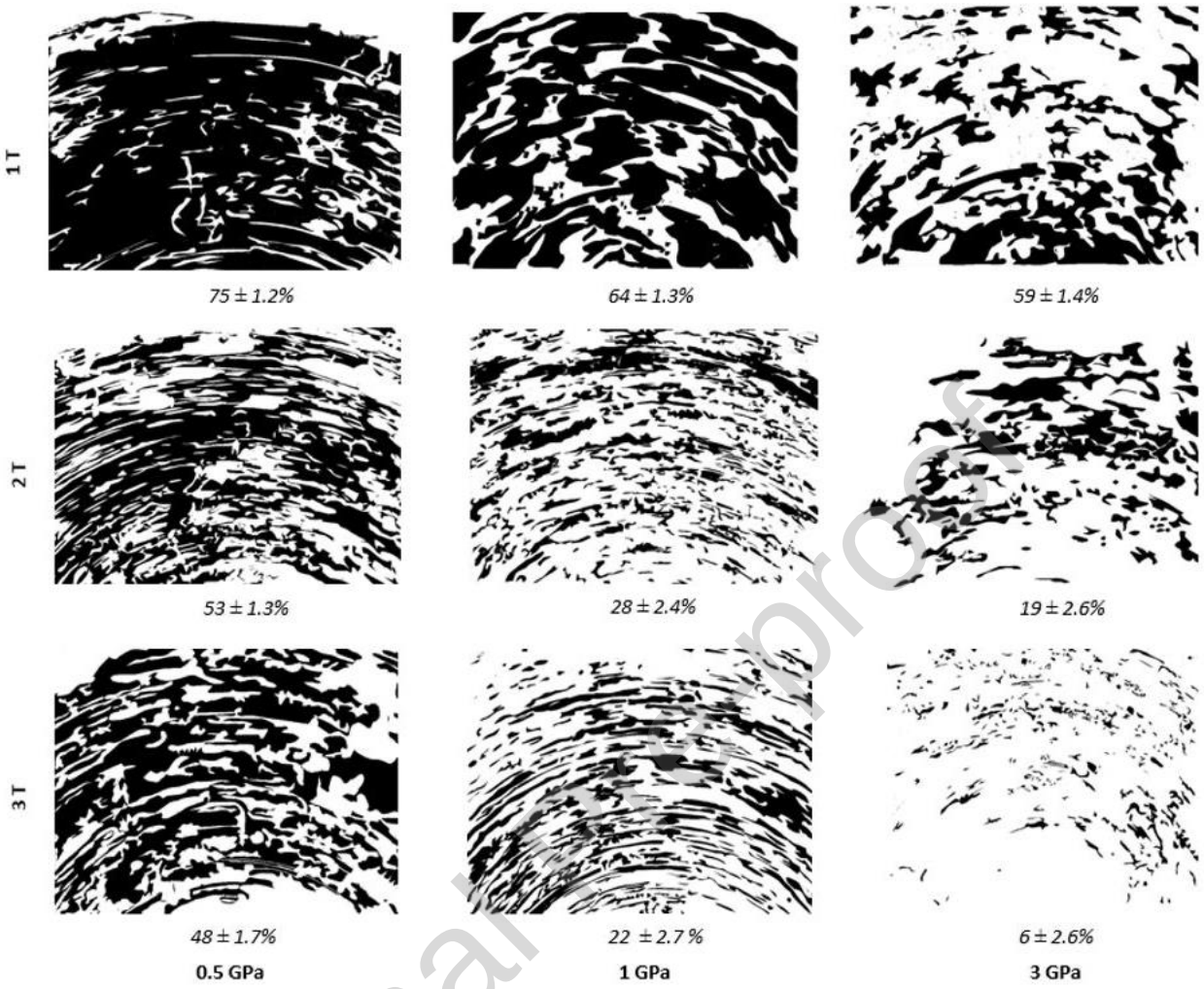

Figure 8. % TWES on the top surface of samples after HPT tests under different conditions. Each image was taken from a group of eight images processed using an IPP.

The amount of TWES on the top surface was quantified using the method shown in Figure 1. The results are summarised in Figure 8 by black / white masks generated by IPP *Image J*. The highest % TWES was registered in samples processed using 0.5 GPa 1 turn (75 ± 1.2 %) and reduced with the number of turns to a very low value (around 6 %) at 3 GPa 3 turns. The amount of TWES varied more with number of turns than with pressure, but in all cases, a significant reduction was reported with increasing turns/pressure.

3.4.2 Region 2, SWES (subsurface).

Circular sections generated by serial polishing from the bottom surface side of the samples revealed white structures located between 240 – 360 µm from the bottom side of the samples. Most of the SWES was found at a radial distance of between 3.5 and 5 mm and no SWES was observed in regions located at a radial distance of less than 3 mm. In samples processed using 3 GPa, a significant increase in the amount of SWES was observed between 1 and 2 turns, but then reduced after applying 3 turns; relatively few SWES were found in samples processed using 6 GPa and 1 turn.

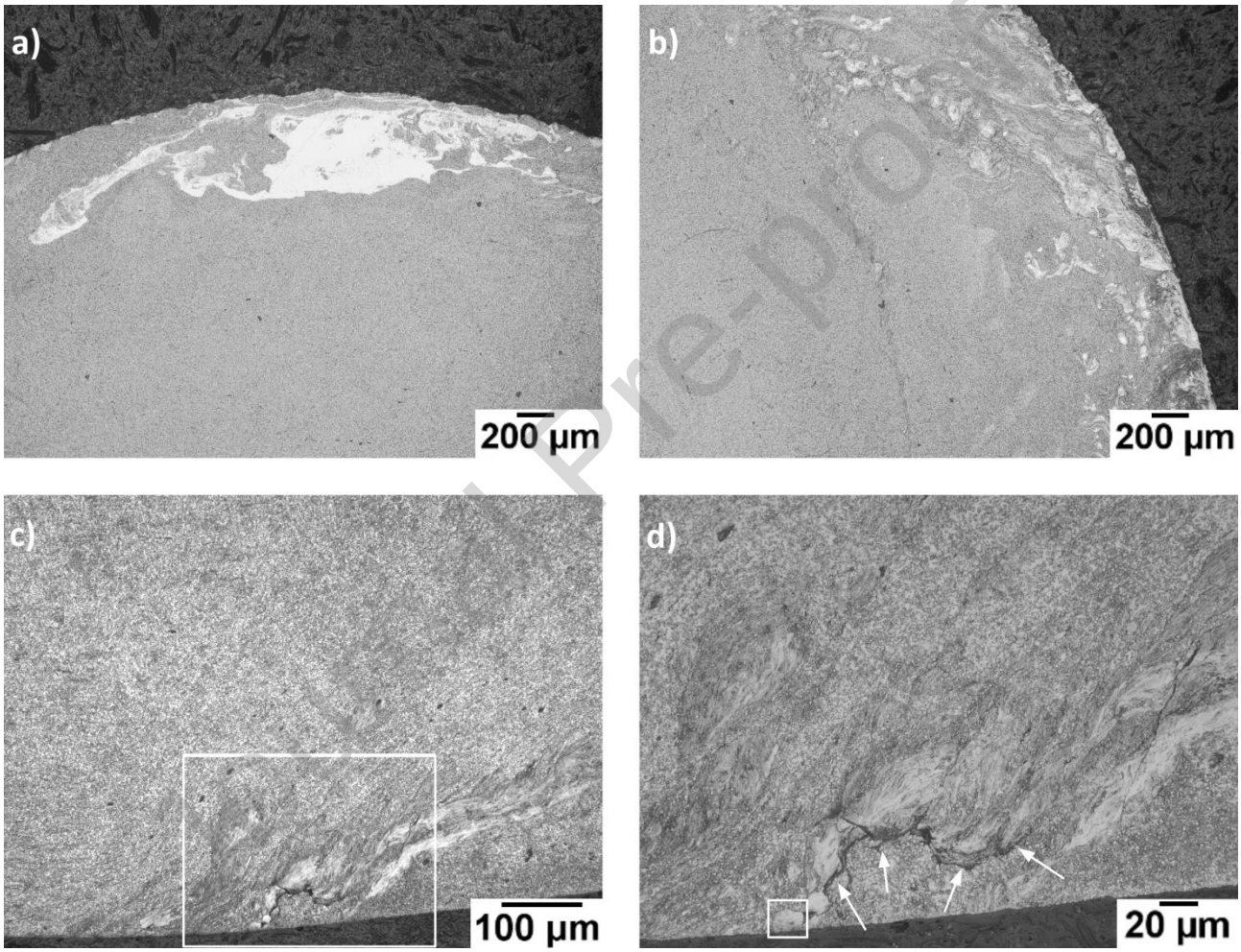

Figure 9. Different SWES configurations found in a disc sample processed using 3 GPa 2 turns. a) Large solid SWES system located between a radial distance of 4.6 mm and the edge of the sample. b) Large cloud SWES system located between a radial distance of 4.6 mm and the edge of the sample. b). c) A large system of cloud and solid SWES at the edge of the HPT sample. d) SWES apparently linked to a crack network (white arrows).

The white rectangle indicates the area shown at higher magnification using SEM / SEI in Figure 11 a). LOM 2 % Nital 2 %.

Two SWES configurations were identified, those with irregular borders and those with more solid areas. The SWES with irregular borders had a swirled morphology and resembled spiral clouds or vortices without clear boundaries, hence they are referred to here as cloud SWES. Similar to the TWES discussed earlier, these cloud SWES usually appeared overlapped by the ferritic matrix (Figure 9 a)). Their size also varied considerably with radial position and tended to be bigger close to the edge of the samples. Moreover, Solid SWES were characterised by their more well-defined borders; their size also increased with radial distance, from isolated spots located at a radial distance of 4 mm to large regions close to or at the edge of the samples (Figure 9 b)). In general, cloud SWES were not located close to the sample edges, whilst most solid SWES were found there. In other cases, cloud and solid SWES appeared joined in complex arrays that extended across large areas until the edge of the samples was reached. Some parts of the clouds appeared as solid, especially those located in the centre of the swirl pattern or close to the edge of the samples. These systems often appeared linked to crack networks which extended for significant distances. In these areas it was not possible to establish a clear difference between clouds and solid structures (Figure 9 c) and d)).

3.5 Nano hardness measurements.

A region located at approximately 4.2 mm radial distance on the top surface of a sample processed by 3 GPa 3 turns visible in the white square in Figure 10 a) was selected for nano-indentation. In this region WES appeared as isolated patches affected by wear, whilst some over-etched regions appeared as dark patches. The nano hardness map produced after taking measurements is shown in Figure 10 b).

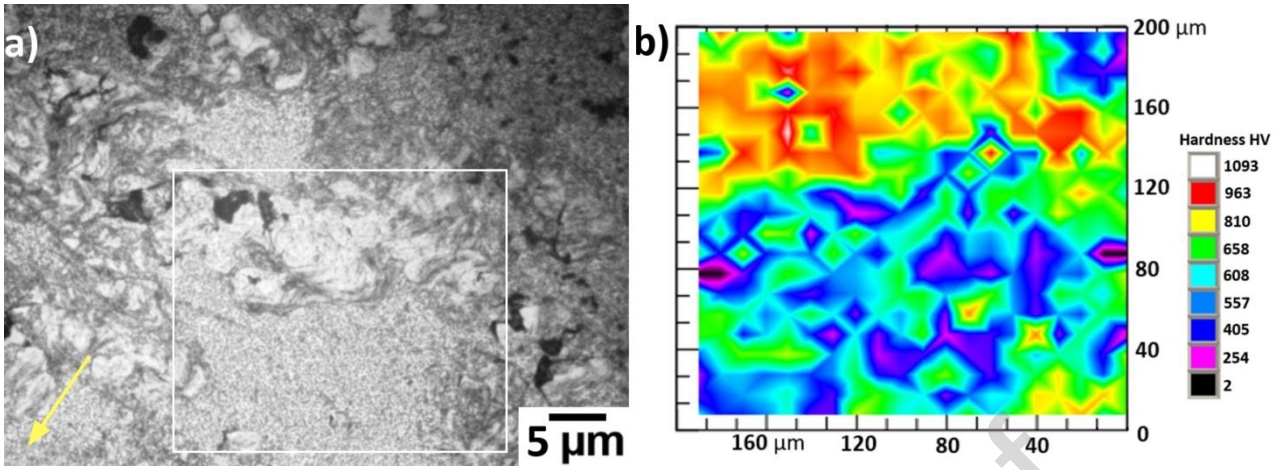

Figure 10. Nano hardness measurements. a). Top surface of a sample processed using 3 GPa 3 turns located at approximately 4.2 mm radial distance. The region selected for nano-hardness measurements is defined in the white square. The yellow arrow indicates the centre of the sample. LOM Nital 2. b). Nano hardness map taken from the area enclosed by the white square shown in a).

The highest nano hardness values were located at the top of the region analysed where the WES were concentrated. The hardness in this region varied predominantly between 658 and 963 HV corresponding to the green, yellow and red colours in the map; there was also an isolated measurement of 1063 HV. The lower hardness values corresponded to regions occupied by the matrix and here the hardness varied predominantly between 405 and 608 HV. The significant variation of the nano hardness values is a consequence of the scale of the nano and micro indents. Nano indents could be located on hard particles such as inclusions, carbides or carbide clusters so generating higher values. On the other hand, different factors could influence the lower measurements, such as indents on ferritic regions free or carbides or the lack of effective contact between the indenter and the material due to roughness variations.

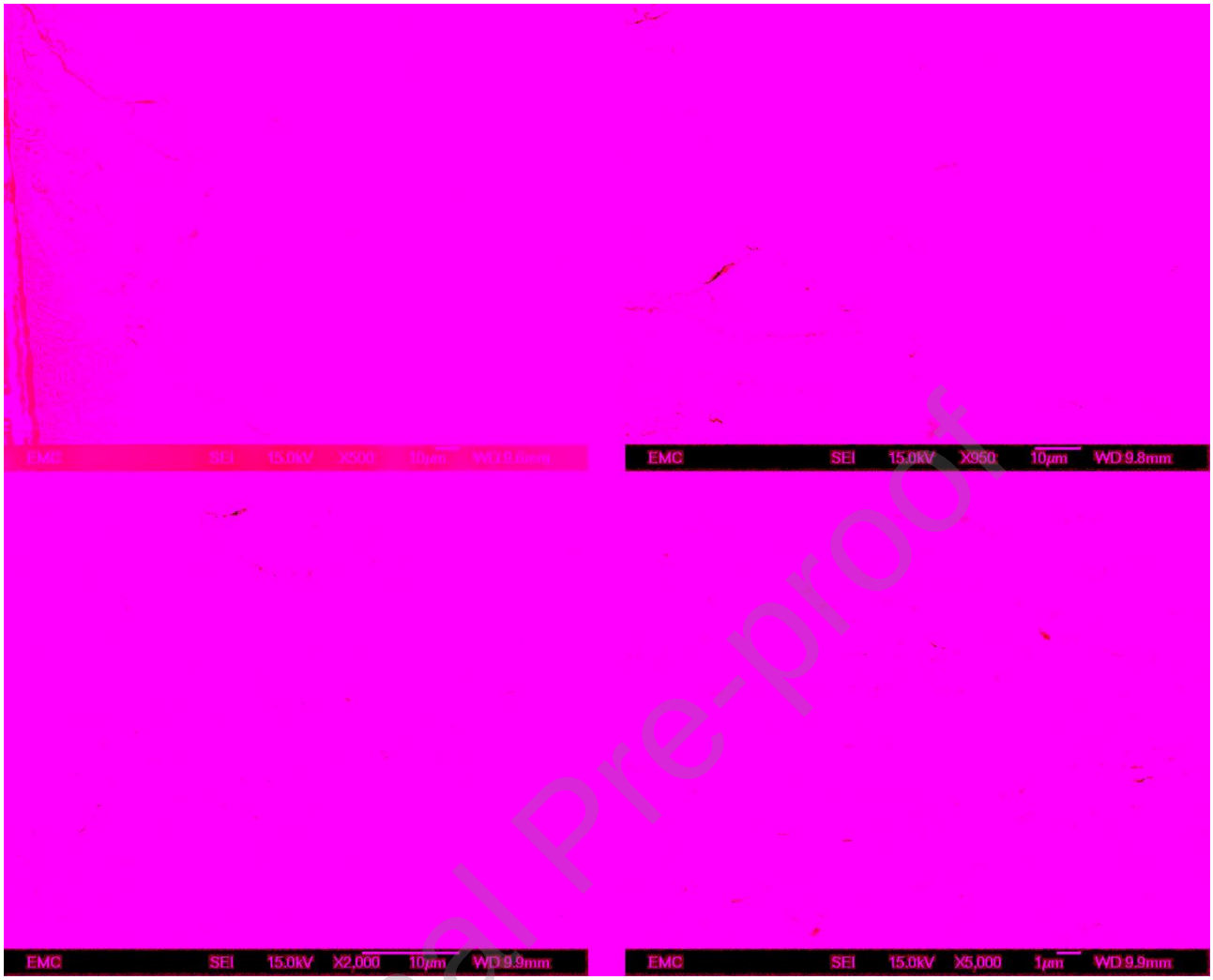

Figure 11. General panorama of a SWES system close to the edge of a HPT sample The white rectangles indicate the area shown at higher magnification in the next figure. a) Solid SWES (enclosed by orange line, region 1) and cloud SWES (enclosed by yellow lines, region 2). b) A fibrous structure is visible in both solid and cloud areas (regions 1 and 2). c) Differences between the carbide distribution in the vicinity of SWES and other random regions. d) Deformed carbides linked to the SWES thin fibres (white arrows). 3 GPa 2 turns SEM / SEI. Nital 2 %.

A detailed examination of the circumferential serial sections prepared through the sample disc revealed more details of the morphology and distribution of SWES. Figure 11 a) was taken from the same region studied by LOM in Figure 9 d) (area enclosed by white rectangle). As was highlighted for TWES, the features described in these figures were observed in all SWES identified, no matter the pressure or number of turns used for the

HPT tests. Figure 11 a) shows a general panorama of the selected SWES system, which consisted of a solid well-defined white region located close to the edge of the sample (enclosed by orange line, region 1) and a group of small and elongated cloud SWES located close by (enclosed by yellow lines). Figures 10 b), c) and d) present details of the same SWES system at higher magnifications. A fibrous structure is visible inside both solid and cloud SWES (regions 1 and 2 in Figure 11 b) and c)). Some cracks were located preferentially in the solid SWES, forming an extended network. SEM / SEI images taken from the clouds and small solid SWES showed a twisted and folded fibrous structure that overlapped the ferritic matrix (Figure 11 c)). The carbide distribution in the vicinity of the SWES differs from the random distribution observed in the ferritic matrix. The carbides seemed to have been dragged by a flow force that surrounded the SWES, some of the carbides appearing deformed and linked to the thin fibres (white arrows in Figure 11 d)).

4. Discussion.

4.1 Slippage and TWES.

TWES only appeared on the top surface of the samples where slippage took place. This suggests that TWES could have formed as a consequence of the sliding taking place between the top surface of the disc and the anvil. Thus, to understand the origin of TWES, it is necessary to study the evolution of slippage. At the beginning of the HPT tests, the pressure imposed embedded the anvil asperities in both top and bottom surfaces of the samples. Once torsion is applied the top surface of the rotating sample slips against the stationary top anvil, and the anvil asperities create grooves and deform the top surface except when the pressure is very high, e.g. at 6 GPa. As a consequence, the circular patterns alternated by smooth and shiny areas were formed. Similar configurations have been reported as a usual feature on HPT samples affected by slippage [42, 43]. Thus, for pressures between 0.5 and 3 GPa the frictional stress between the top rotating surface of the sample and the anvil will be below the shear yield stress of the sample and slippage occurs. Localized plastic flow takes place because of asperities sliding and the circular pattern features observed on the sample surface are formed. When the pressure is increased, the frictional stress will also increase and at a certain point it will reach the shear yield stress producing "*sticking*" between the surfaces in contact. Hence, as the

applied pressure increases the slippage starts to reduce and the circular patterns reduce significantly until they disappear [44, 45]. Significant % slippage reductions have been reported experimentally in Al, Cu and Fe when pressures are increased from 2 to 6 GPa. In the annealed AISI 52100 steel samples studied here the % slippage also reduced significantly as the pressure increased from 1 to 6 GPa (Figure 8). The transition from slippage to “sticking” is gradual, hence, to avoid any slippage, and the formation of TWES associated with it, high-pressures (3.5 – 5 GPa) and relatively high roughness of the anvils (approximately 30 µm Ra) have been recommended [46].

4.2 The role of surface roughness.

Nevertheless, the process described above cannot be used to explain the interaction between the bottom surface of the samples which reproduced the anvil roughness in all cases, generating *orange peel* patterns. A similar surface configuration has been described in a previous study, where the roughness of the anvils used to process stainless steels were carefully characterised [43]. Based on this examination it was concluded that the *orange peel* impression occurred on the lower surface of the disc because the roughness of the bottom anvil was higher than the top anvil. At this point, the roughness impressions taken from the samples pressed using the HPT test machine can help. Roughness measurements on these surfaces indicated that the top sample surfaces in contact with the stationary top anvil had smaller values of all parameters evaluated (Ra, Rq, Rz) than the lower surface in contact with the rotating anvil (the results of these measurements are summarised in Table 2). Figure 12 also shows that areas of the top surface had no impression of the anvil indicating that over some areas of the top surface of the disc there was no contact between anvil and sample when only compression was applied, thus no frictional forces in these areas and hence slippage is easier. This lack of contact across some of the top surface of the sample might result from two factors: the top and bottom surfaces not being completely parallel, and the anvils having suffered significant wear after a certain time of usage. When torsion is applied sufficient deformation of the sample occurs so that contact is then made across all the surface, friction increases and slippage decreases.

Table 2. Roughness measurements taken from the disc samples after being compressed in the HPT test machine. UP refers to an unprocessed sample. Values are the average of five measurements (Ra ± 0.5 µm, Rq ± 0.2 µm, Rz ± 2.1 µm)

	Top surface (UP)	**Bottom surface (UP)**	**Top surface 1 GPa**	**Bottom surface 1 GPa**	**Top surface 3 GPa**	**Bottom surface 3 GPa**	**Top surface 6 GPa**	**Bottom surface 6 GPa**
Ra (µm)	0.18	0.16	2.62	3.64	2.69	4.14	2.6	3.95
Rq (µm)	0.25	0.22	3.28	4.39	3.38	4.88	3.29	4.87
Rz (µm)	1.73	1.62	15.04	19.14	15.6	20.86	14.97	22.14
Ra interval (µm)	0.1 - 2	0.1 - 2	2 - 10	3 – 10	4 to 10	5 - 10	6 -10	7 – 10
Rz interval (µm)	0.5 -10	0.5 to 10	10 - 50	11 – 50	12 -50	13 - 50	14 -50	15 – 50
Cut off λc (mm)	0.8	0.8	2.5	2.5	2.5	2.5	2.5	2.5
Length	4	4	12.5	12.5	12.5	12.5	12.5	12.5

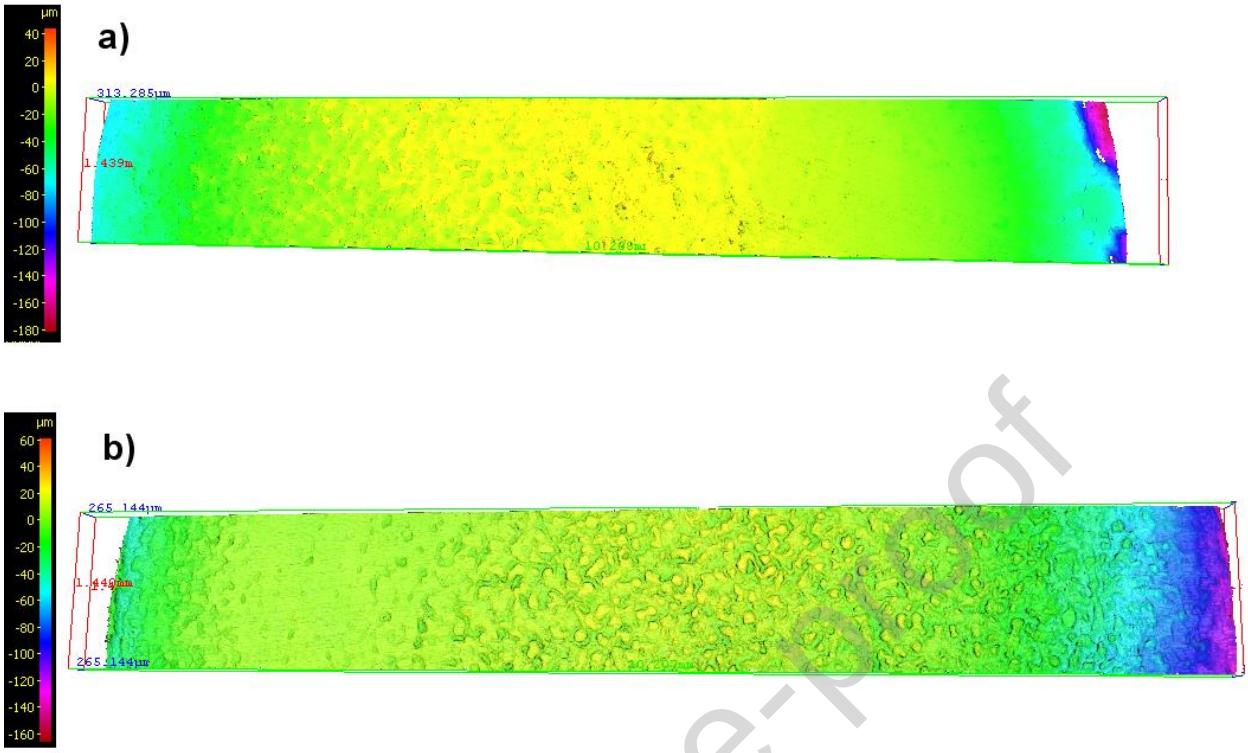

Figure 12. Reconstruction of a) top and b) bottom anvil surfaces along the diameter of a sample disc pressed under 1 GPa. The roughness on the top surface is less than that of the bottom surface (See Table 2). Note the large smooth area at the right of the top surface of the sample, and the orange peel pattern at the centre of the bottom surface.

The lower roughness of the top anvil could act to produce lower friction forces on the top surface and thus aid slippage and the generation of TWES. On the contrary, because the bottom surface of the anvil has a higher roughness and complete contact over all the surface, the pressures applied were sufficient to generate higher friction forces and slippage did not occur on the bottom surface side. The amount of TWES decreased when the number of turns was increased; this could result from material detaching from the top surface during the rotation because of severe sliding wear. It is clear that TWES have higher hardness than the matrix, but less than the anvil asperities. If these asperities slide against the TWES after one or more turns, they could detach these areas eventually producing wear debris that becomes trapped between the surfaces in contact, generating a three-body wear system [47]. Figure 7 shows some of the debris collected from the top

anvil after conducting HPT tests, typical sliding wear features appear on their surfaces as has been reported before [48].

4.3 TWES formation.

TWES consisted of a fibre / layered structure that extended parallel to the top surface in some regions but containing swirls or vortices in other places. The origin of the fibres / layers seems to be related to the strain and plastic flow caused by the interaction between anvil asperities and the sample surface during the slippage. As their geometry was not regular, anvil asperities could create heterogeneous flow conditions in very localized places causing small neighbouring regions to flow under different conditions, generating *interactions* between them. As a result, the *interactions* could produce shear instabilities, atomic scale mixing, and the generation of nano eddies or vortices at the sliding interfaces [49, 50].

As a consequence, the interface between the neighbouring regions could change to nano fibres / layers with different mechanical properties [51]. The primary nature of these fibres / layers in the annealed AISI 52100 is not completely understood but could be related to transformation mechanisms observed under SPD conditions, such as segregation and diffusion of interstitial elements through “non-equilibrium” grain boundaries [52], the formation of high-density dislocation clusters (called by some authors dislocation cores) and the generation of new structures by dynamic recrystallization [20]. These processes might be influenced by any heat generated by HPT such as that resulting from plastic deformation of the sample, sample / anvil friction, and flash formation. Any resultant temperature rise could affect the evolution of the fibre / layered structure and the vortices described above. However, according to previous experimental and FEM studies the effect of temperature rise can be considered negligible due to three main factors: the heat sink effect resulting from the large mass of the anvils compared to the sample discs, the small temperature increments, and the HPT parameters used in the tests. Firstly, the heat generated is dissipated by conduction from the sample to the anvil and by convection / emission from the HPT machine to the environment [53, 54]. Secondly, plastic deformation as the main heating source, generates little heating and gives rise to temperatures far below any steel transformation temperature [53-55, 56]. Thirdly, parameters such as the

low rotational speed and short processing time (1 rpm and between 1 and 3 minutes), low final strain (up to 3 turns on 0.98 mm diameter samples) [56], and a soft material processed (180 ± 10 HV for the annealed AISI 51200) [55], would also limit greatly the temperature rise in the sample discs processed by HPT. As slippage progressed, new fibres / layers were formed and stacked over each other. Different flow conditions could appear between the deformed matrix and the stacked fibres, recreating new heterogeneous flow conditions. Thus, the process described above could take place several times until structures on a micro scale are produced. The differences between the mechanical properties of these new fibre / layered structures (TWES and SWES hardness were higher than the adjacent ferritic matrix) could also explain the beginning of small cracks around the fibre / layered structures (white arrows in Figure 6 a)). The soft ferrite could tend to flow more easily around them than through them. This movement could continue until the brittle interface cannot support the flow and the excess energy accumulated during the sliding is liberated through crack formation. At higher strains, bigger vortices appeared affecting ever-larger regions, preferentially close to the edges of the samples. The vortices by themselves could provide more conditions where more *interactions* take place to generate new fibres / layers and so extend the WES. The nature of these bigger vortices is not related directly to the atomic interaction and will be discussed later for the SWES case. However, voids and cracks could progress creating bigger crack networks on a micro scale and are possibly responsible for the detachment of significant portions of the deformed surface.

Based on these observations, it would appear that the shear stress promoted by the slippage was responsible for the transformation of the ferrite matrix and carbides located close to and inside the TWES. This transformation could include grain refinement and diffusion of carbon from the carbides to the deformed matrix. Similar transformations have been considered to explain the formation of white layers in AISI 52100 in hard turning [57-59] and drilling [60] machining processes at temperatures below any phase transformation, i.e., without static recrystallization promoted by high temperatures. Similar conditions also have been claimed to describe the microstructural evolution of railway steels under rolling-sliding contact loading [61, 62].

4.4 SWES formation

The strain in HPT tests is estimated by a simple model to be constant throughout the thickness of the sample discs but changes linearly with radial distance [23]. Thus, variations in the mechanical properties or microstructure are not expected in the thickness direction, i.e. on surfaces of axial sections. This model has good experimental support when the materials have reached a saturated condition, usually after applying High-Pressure s and several turns, however significant differences appear when low strains are imposed.

Some studies in Mg, Al, Zr_3Al, iron and pearlitic steels have shown dissimilarities in terms of hardness distribution and microstructural changes across the axial sections of samples which suggests a non-homogeneous strain distribution inside the samples and changes in the plastic flow [63 – 65]. Moreover, FEM simulations have reported concentration of the strain at the centre of the diametral axial section, with the highest values at the edge. The strain rate also appeared greater in this region, with values increasing with radial distance [66]. The parameters used to conduct the HPT tests did not allow a completely refined grain structure with similar mechanical properties to be achieved. On the contrary, the samples showed microstructural changes across the whole thickness, such as evidence of localised high plastic deformation in the ferritic matrix, cracks and the formation of the subsurface white structures (SWES). These SWES, indicated by white arrows in Figure 13, seem to be concentrated at the sample mid-thickness and between a radial distance of 3.5 mm and the edge of the sample.

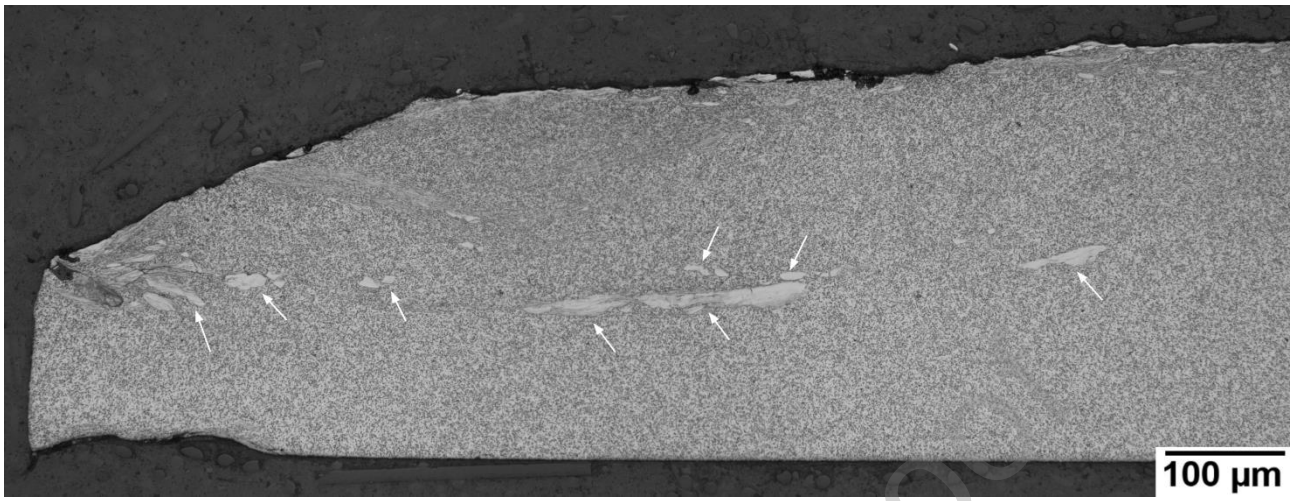

Figure 13. An axial section of a disc sample processed using 3 GPa 2 turns, showing SWES at radial distances of between 3.5 mm and the edge of the sample (white arrows). LOM Nital 2 %.

The sample thickness was originally 0.8-0.9 mm and was reduced to around 0.7-0.6 mm during the HPT test. As that higher strain allows conditions to generate white structures (as was discussed in the TWES case), the concentration of SWES at the edge of the samples could be justified [67, 68]. However, the plastic flow at the edge of the sample can vary significantly due to other complex factors, such as the friction between the flash and anvils outside of the anvil cavities, the friction against the vertical cavity walls, or the formation of dead metal zones [69, 70]. Hence, the study of plastic flow in this region is complex.

4.5 SWES fibre / layered structure

Figures 11 a) to d) show structures that resemble vortices created by turbulence in fluids. Similar flow patterns have been observed in previous HPT tests conducted on high-purity aluminium and a Zn–22%Al eutectoid alloys [71] and magnesium AZ80 alloy [72]. In these tests, structures such as swirls or vortices and tracks of *local turbulence* that resembled the vortices associated with Kelvin–Helmholtz instabilities in fluids were identified.The instabilities could occur where there are local shear velocity gradients between adjacent positions. However, the Kelvin–Helmholtz instabilities requires inertial forces in rapidly

flowing low viscous fluids at high Reynolds numbers, and metals flow with very small Reynolds number because of their high viscosities and very low flow velocities. Therefore, this hypothesis cannot explain the vortices registered in HPT sample discs. Some authors have suggested that the origin of vortices could be linked to dislocation-mediated plastic flow, with suitably oriented slip systems. Subsequent folding could be explained by the inhomogeneity of plasticity on polycrystalline surfaces which favours bulge formation on a scale of the grains [71]. However, the vortices observed are much larger than any grains, suggesting that another factor must be related to their evolution. Jiang W. et al. they have provided experimental evidence supporting the vortex formation is related to the presence of well-developed grains and/or nano-crystalline structures [72]. Other studies, based on computational simulations, have suggested that some *obstacles* could block the shear deformation and generate swirls and coils [73, 74]. Experimental evidence of this phenomenon has been used to account for the decomposition of spheroidal cementite immersed in a martensite matrix of an AISI 52100 bearing steel processed by HPT. The softer matrix flows around the harder spheroidal carbides, dragging C and Cr due to a wear effect registered at the matrix-cementite interface [20]. The plastic flow patterns around cementite particles resembled small coils which could be the origin of bigger vortices, higher C and Cr dissolution rates and hence, a possible driver for the initiation of WEAs. However, in this study no white etching structure similar to WEAs were produced by HPT. The nature of the obstacles in the present case (annealed AISI 5210 processed by HPT) is not completely clear, although they could be related to hard bodies inside the matrix such as non-metallic inclusions or carbide clusters. Advanced characterisation methods such as Electron Backscatter Diffraction (EBSD) and / or Energy-dispersive X-ray spectroscopy (EDS) could help to identify or discard the presence of these atypical bodies and their role in the formation of vortices and SWES.

5. Conclusions.

WES, similar to the WEAs found in failed rolling bearings affected by WSF, were revealed after conducting HPT tests on annealed AISI 52100 bearing steel. These WES were observed in two main regions: close to the top surface at a radial distance of between 1.5 mm and 5 mm (TWES), and subsurface in a region located approximately 250-350 µm

from the bottom surface of samples at a radial distance of between 3.5 mm and the edge of the samples (SWES).

TWES covered the top surfaces as an irregular layer that was confined to a region within 100 μm of the surface. They consisted of a fibre / layered structure that extended parallel to the surface in some regions but contained swirls or vortices in other places. SWES varied in size and shape with radial distance, from spots with irregular borders to well defined solid structures. The regions with irregular borders which looked similar to swirled clouds (cloud SWES) appeared in various regions in random patterns. Solid SWES appeared largely at the edge of the samples. Both TWES and SWES, share similar features such as fibre / layered internal structure, higher hardness compared to the deformed ferritic matrix that surrounds them, and the absence of the carbide distribution observed in the matrix.

Different drivers have been suggested to explain the origin of WES. For TWES, the sliding of the asperities on the top anvil against the sample created heterogeneous flow conditions in small neighbouring regions and instabilities between them. For SWES, the interruption of the plastic flow due to hard bodies such as non-metallic inclusions or carbide clusters, could create vortices. These vortices may be responsible for the initiation and growth of WES. Vortices could act also close to the edge of the samples, where other factors, such as influence of dead metal zones, lateral friction and flash formation helped to create more complex flow conditions.

The drivers described above share a common factor: the interactions between small neighbouring regions that flow under different conditions. The local shear instabilities, atomic scale mixing, and the generation of nano eddies or vortices at the sliding interfaces generated between them could promote the movement of carbon from carbides to the ferritic matrix and hence contribute to their dissolution. Similar transformation mechanisms could operate in other materials under different SPD conditions, such as those present in quenched/tempered bearing steels working in rolling contact fatigue regimes.

Acknowledgments.

This research has been co-funded by the National Centre of Advanced Tribology at Southampton – nCATS at the University of Southampton (UK), the Universidad EIA (Envigado, Antioquia Colombia), the Colombian Administrative Department of Science, Technology and Innovation – Colciencias (Colombia), and the Agency for Higher Education - Sapiencia, Enlazamundos Program (Colombia).

References.

[1] M.N. Kotzalas, G.L. Doll

Tribological Advancements for Reliable Wind Turbine Performance

Philosophical Transactions of the Royal Society A: Mathematical, Physical and Engineering

Sciences

Vol. 368 (1929) (2010), pp. 4829–4850

[2] M. H. Evans

White Structure Flaking (WSF) in Wind Turbine Gearbox Bearings: Effects of 'Butterflies' and White Etching Cracks (WECs)

Materials Science and Technology

Vol. 28 (1) (2012), pp.3-22

[3] L. Zepeng, L. Zhang.

A Review of Failure Modes, Condition Monitoring and Fault Diagnosis Methods for Large-Scale Wind Turbine Bearings

Measurement

Vol. 149 (2020), Article 107002

[4] A. Greco, S. Sheng, J. Keller, A. Erdemir

Material Wear and Fatigue in Wind Turbine Systems

Wear

Vol. 302 (1-2) (2013), pp. 1583-1591

[5] A. Grabulov, U. Ziese, H. W. Zandbergen

TEM/SEM Investigation of Microstructural Changes within the White Etching Area under Rolling Contact Fatigue and 3-D Crack Reconstruction by Focused Ion Beam

Scripta Materialia

Vol. 57 (7) (2007), pp. 635-638

[6] H.A. Al-Tameemi, H. Long

Finite Element Simulation of Subsurface Initiated Damage from Non-Metallic Inclusions in Wind Turbine Gearbox Bearings

International Journal of Fatigue

Vol.131 (2020), Article 105347

[7] M.-H. Evans, J.C. Walker, C. Ma, Wang, R.J.K. Wood

A FIB/TEM Study of Butterfly Crack Formation and White Etching Area (WEA) Microstructural Changes under Rolling Contact Fatigue in 100Cr6 Bearing Steel

Materials Science and Engineering

Vol. 570 (2013), pp. 127–134

[8] G. Guetard, I. Toda-Caraballo, P.E.J. Rivera-Díaz-del-Castillo

Damage Evolution Around Primary Carbides Under Rolling Contact Fatigue in VIM–VAR M50

International Journal of Fatigue

Vol. 91(1) (2016), pp. 59-67

[9] K. Sreeraj, P. Ramkumar

Comprehensive Analysis of Effects of Dynamic Load Frequency and Hydrogenation to Instigate White Etching Areas (WEAs) Formation under Severe Sliding Condition of Bearing Steel

Tribology International

Vol. 144 (2020), Article 106131

[10] M. Paladugu, R. Scott

White Etching Matter Promoted by Intergranular Embrittlement

Scripta Materialia

Vol. 130 (2017), pp. 219-222

[11] M. Paladugu, R. S. Hyde

Microstructure Deformation and White Etching Matter Formation along Cracks

Wear,

Vol. 390–391 (2017), pp. 367-375

[12] L. Morsdorf, D. Mayweg, Y. Li, A. Diederichs, D. Raabe, M. Herbig

Moving Cracks Form White Etching Areas during Rolling Contact Fatigue in Bearings

Materials Science and Engineering

Vol. A 771 (2020), Article 138659

[13] Y. J. Li, M. Herbig, S. Goto, D. Raabe

Atomic Scale Characterization of White Etching Area and its Adjacent Matrix in a Martensitic 100Cr6 Bearing Steel

Materials Characterization

Vol. 123 (2017), pp. 349–353

[14] V. Smelova, A. Schwedt, L. Wang, W. Holweger, J. Mayer

Microstructural Changes in White Etching Cracks (WECs) and their Relationship with those in Dark Etching Region (DER) and White Etching Bands (WEBs) due to Rolling Contact Fatigue (RCF)

International Journal of Fatigue

Vol. 100 (2017), pp. 148–158

[15] D. Mayweg, L. Morsdorf, Y. Li, M. Herbig

Correlation Between Grain Size and Carbon Content in White Etching Areas in Bearings

Acta Materialia

Vol. 215 (2021), Article 117048

[16] D. Mayweg, L. Morsdorf, X. Wu, M. Herbig

The Role of Carbon in the White Etching Crack Phenomenon in Bearing Steels

Acta Materialia

Vol. 203 ((2021), Article 116480

[17] H. K. Danielsen, C. Hong, O.V. Mishin

Microstructural Characterization of White Etching Cracks in Bearings after Long-Term Operation in Wind Turbines

Materials Letters

Vol. 294 (2021), Article 129754

[18] F. J. López-Uruñuela, B. Fernández-Díaz, F. Pagano, A. López-Ortega, B. Pinedo, R. Bayón, J. Aguirrebeitia

Broad Review of "White Etching Crack" Failure in Wind Turbine Gearbox Bearings: Main Factors and Experimental Investigations

International Journal of Fatigue

Vol. 145 (2021), Article 106091

[19] J. Spille, J. Wranik, S. Barteldes, J. Mayer, A. Schwedt, M. Zürcher, T. Lutz, L. Wang, W. Holweger

A Study on The Initiation Processes of White Etching Cracks (WECs) in AISI 52100 Bearing Steel

Wear

(2021) Article 203864

[20] Y. Ivanisenko, W. Lojkowski, R. Z. Valiev, H. J. Fecht

The Mechanism of Formation of Nanostructure and Dissolution of Cementite in a Pearlitic Steel during High-Pressure Torsion

Acta Materialia

Vol. 51 (18) (2003), pp. 5555-5570

[21] Y. Qin, D. Mayweg, P.Y. Tung, R. Pippan, M. Herbig

Mechanism of Cementite Decomposition in 100Cr6 Bearing Steels During High-Pressure Torsion

Acta Materialia

Vol. 201 (2020), pp. 79-93

[22] H. Zhu, H. Li, A. Al-Juboori, D. Wexler, C. Lu, A. McCusker, J. McLeod, S. Pannila, J. Barnes

Understanding and Treatment of Squat Defects in a Railway Network

Wear

Vol. 442–443 (2020), Article 203139

[23] T.G. Langdon

Twenty-five Years of Ultrafine-grained Materials: Achieving Exceptional Properties through Grain Refinement

Acta Materialia

Vol. 61 (19) (2013), pp. 7035-7059

[24] H. K. D. H. Bhadeshia

Steels for Bearings

Progress in Materials Science

Vol. 57 (2) (2012), pp. 268 - 435

[25] J. Jelita Rydel, I. Toda-Caraballo, G. Guetard, P.E.J. Rivera-Díaz-del-Castillo

Understanding the Factors Controlling Rolling Contact Fatigue Damage in VIM-VAR M50 Steel

International Journal of Fatigue

Vol. 108 (2018), pp. 68-78

[26] British Standard Institution

% Carbon – Chromium Steel Billets, Bars, Forging and Parts (Limiting Ruling Section 25 mm)

BSI Standard Publication

BSI 2S 135:1977 London - England - UK (2009), pp. 1-25.

[27] Simply-Bearing

AISI 52100 Chrome Steel Needle Roller Data Sheet.

https://simplybearings.co.uk/shop/files/52100_roll.pdf, 2015 (accessed 06/04/2017).

[28] K. Edalati, D. J. Lee, T. Nagaoka, A. Makoto, Kim, S.K. Hyoung, Z. Horita, R. Pippan

Real Hydrostatic Pressure in High-Pressure Torsion Measured by Bismuth Phase Transformations and FEM Simulations

Materials Transactions

Vol. 57 (4) (2016), pp. 533-538

[29] D.M. Marulanda Cardona, J. Wongsa-Ngam, T.G. Langdon

Microstructural Evolution and Microhardness in a Low Carbon Steel Processed by High-Pressure Torsion

Journal of Materials Research and Technology

Vol. 3 (4) (2014), pp. 344-348

[30] Y. Mine, Z. Horita, Y. Murakami

Effect of Hydrogen on Martensite Formation in Austenitic Stainless Steels in High-Pressure Torsion

Acta Materialia

Vol. 57(10) (2009), pp. 2993-3002

[31] Y. Mine, Z. Horita, Y. Murakami

Effect of High-Pressure Torsion on Hydrogen Trapping in Fe–0.01 mass% C and type 310S Austenitic Stainless Steel

Acta Materialia

Vol. 58 (2) (2010), pp. 649-657

[32] Y. Liu, X. Bian, K. Zhang, C. Yang, L. Feng, H.S. Kim, J. Guo

Interfacial Microstructures and Properties of Aluminium Alloys / Galvanized Low-Carbon Steel under High-Pressure Torsion

Materials & Design

Vol. 64 (2014), pp. 287-293

[33] S. Scheriau, Z. Zhang, S. Kleber, R. Pippan

Deformation Mechanisms of a Modified 316L Austenitic Steel Subjected to High Pressure Torsion

Materials Science and Engineering

Vol. 528(6) (2011), pp. 2776-2786

[34] M.S. Matoso, R.B. Figueiredo, M. Kawasaki, D.B. Santos, T.G. Langdon Processing a **Twinning-Induced Plasticity Steel by High-Pressure Torsion**

Scripta Materialia

Vol. 67(7) (2012), pp. 649-652

[35] F. J. Kalahroudi, H. Koohdar, H.R. Jafarian, Y. Haung, T.G. Langdon, M. N. Ahmadabadi

On the Microstructure and Mechanical Properties of an Fe-10Ni-7Mn Martensitic Steel Processed by High-Pressure Torsion

Materials Science and Engineering

Vol. 749 (2019), pp. 27-34

[36] M. Busquet, S. Descartes, Y. Berthier

Formation Conditions of Mechanically Modified Superficial Structures for Two Steels

Tribology International

Vol. 42(11) (2009), pp. 1730-1743

[37] E.G. Astafurova, M.S. Tukeeva, G.G. Maier, E.V. Melnikov, H.J. Maier

Microstructure and Mechanical Response of Single-crystalline High-manganese Austenitic Steels under High-Pressure Torsion: The Effect of Stacking-Fault Energy

Materials Science and Engineering

Vol. 604 (2014), pp. 166-175

[38] K. Edalati, Z. Horita, T. G. Langdon

The Significance of Slippage in Processing by High-Pressure Torsion

Scripta Materialia

Vol. 60 (1) (2009), pp. 9-12

[39] W. S. Rasband

ImageJ,

U. S. National Institutes of Health, Bethesda, Maryland, USA, 1997-2018

https://imagej.nih.gov/ij/, (accessed 15/05/2015).

[40] British Standard Institution

Geometric Product Specification (GPS) – Surface Texture –Profile Method: Rules and Procedures for the Assessment of Surface Texture

BSI Standard Publication

BS EN ISO 4288:1998 London - England - UK (1998), pp. 1-18.

[41] N. Wang, L.V. Wilches Pena, L. Wang, B.G. Mellor, Y. Huang

Experimental and Simulation Studies of Strength and Fracture Behaviours of Wind Turbine Bearing Steel Processed by High-Pressure Torsion

Energies

Vol. 9 (12) (2016), pp. 1-13

[42] Y. Cao, Y.B. Wang, R.B. Figueiredo, L. Chang, X. Z. Liao, M. Kawasaki, W.L. Zheng, S.P. Ringer, T.G. Langdon, Y.T. Zhu

Three-Dimensional Shear-Strain Patterns Induced by High-Pressure Torsion and their Impact on Hardness Evolution

Acta Materialia

Vol. 59(10) (2011), pp. 3903-3914

[43] Y. Huang, A. Al-Zubaydi, M. Kawasaki, T.G. Langdon

An Overview of Flow Patterns Development on Disc Lower Surfaces when Processing by High-Pressure Torsion

Journal of Materials Research and Technology

Vol. 3 (4) (2014), pp 303-310

[44] D. Kuhlmann-Wilsdorf, B. C. Cai, R.B. Nelson

Plastic Flow between Bridgman Anvils under High-Pressure

Journal of Materials Research

Vol. 6 (12) (1991), pp. 2547-2564

[45] R.E. Riecker, L.C. Towle

Shear Strength of Grossly Deformed Cu, Ag, and Au at High-Pressure s and Temperatures

Journal of Applied Physics

Vol. 38 (13) (1967), pp. 5189-5194

[46] K. Edalati, K. Horita

A Review on High-Pressure Torsion (HPT) from 1935 to 1988

Materials Science and Engineering

Vol. 652 (2016), pp. 325-352

[47] Z. Gahr

Microstructure and Wear of Materials

Elsevier Science Publisher B.V.

(1987), pp. 80-104

Amsterdam, The Nederlands

[48] W. Hong, W. Cai, S. Wang, M.M. Tomovic

Mechanical Wear Debris Feature, Detection, and Diagnosis: A Review

Chinese Journal of Aeronautics

Vol. 31(5) (2018), pp. 867-882

[49] D.A. Rigney, S. Karthikeyan

The Evolution of Tribomaterial During Sliding: A Brief Introduction

Tribology Letters

Vol. 39 (1) (2010), pp. 3-7

[50] N.K. Sundaram, Y. Guo, S. Chandrasekar

Mesoscale Folding, Instability, and Disruption of Laminar Flow in Metal Surfaces

Physical Review Letters

Vol. 109 (10) (2012), pp. 1-5

[51] H. J. Kim, S. Karthikeyan, D. Rigney

A Simulation Study of the Mixing, Atomic Flow and Velocity Profiles of Crystalline Materials During Sliding

Wear

Vol. 267 (5) (2009), pp. 1130-1136

[52] X. Sauvage, G. Wilde, S.V. Divinski, Z. Horita, R. Z. Valiev

Grain Boundaries in Ultrafine Grained Materials Processed by Severe Plastic Deformation and Related Phenomena

Materials Science and Engineering:A

Vol. 540 (2012), pp. 1-12

[53] R. Figueiredo 52

Using Finite Element Modeling to Examine the Temperature Distribution in Quasi-Constrained High-Pressure Torsion

Acta Materialia

Vol. 60 (2012), pp. 3190–3198

[54] K. Edalati, Y. Hashiguchi, P. H. R. Pereira, Z. Horita, T. G. Langdon. 53

Effect of Temperature Rise on Microstructural Evolution During High-Pressure Torsion

Materials Science and Engineering: A

Vol. 714 (2018), pp.167-171

[55] P.H.R. Pereira, R.B. Figueiredo, Y. Huang, P.R. Cetlin, T.G. Langdon,

Modeling the Temperature Rise in High Pressure Torsion

Materials Science and Engineering

Vol. A 593 (2014) 185-188.

[56] K. Edalatia, R. Miresmaeilic, Z. Horita, H, Kanayamad, R. Pippan 54

Significance of Temperature Increase in Processing by High-Pressure Torsion Materials

Science and Engineering: A

Vol. 528 (2011), pp. 7301– 7305

[57] S. B. Hosseini, T. Beno, U. Klement, J. Kaminski, K. Ryttberg

Cutting Temperatures During Hard Turning—Measurements and Effects on White Layer Formation in AISI 52100

Journal of Materials Processing Technology

Vol. 214 (6) (2014), pp. 1293-1300

[58] Z. Liao, A. La Monaca, J. Murray, A. Speidel, D. Ushmaev, A. Clare, D. Axinte, R. M'Saoubi

Surface Integrity in Metal Machining - Part I: Fundamentals of Surface Characteristics and Formation Mechanisms

International Journal of Machine Tools and Manufacture

Vol. 162 (2021), Article 103687

[59] A. La Monaca, J. W. Murray, Z. Liao, A. Speidel, J A. Robles-Linares, Dragos A. Axinte, M. C. Hardy, A. T. Clare

Surface Integrity in Metal Machining - Part II: Functional Performance

International Journal of Machine Tools and Manufacture

Vol. 164 (2021), Article 103718

[60] J.G.Li, M.Umemoto, Y.Todaka, K.Tsuchiya

Nanocrystalline Structure Formation in Carbon Steel Introduced by High-Speed Drilling.

Materials Science and Engineering: A

Vol. 435-436 (2006), pp. 383-388

[61] Y. Hu, L. Zhou, H.H. Ding, R. Lewis, Q.Y. Liu, J. Guo, W.J. Wang

Microstructure Evolution of Railway Pearlitic Wheel Steels under Rolling-Sliding Contact Loading

Tribology International

Vol. 154 (2021), Article 106685

[62] C.G. He, H.H. Ding, L.B. Shi, J. Guo, E. Meli, Q.Y. Liu, A. Rindi, Z.R. Zhou, W.J. Wang

On the Microstructure Evolution and Nanocrystalline Formation of Pearlitic Wheel Material in a Rolling-Sliding Contact

Materials Characterization

Vol. 164 (2020), Article 110333

[63] A. Hohenwarter, A. Bachmaier, B. Gludovatz, S. Scheriau, R. Pippan

Technical Parameters Affecting Grain Refinement by High-Pressure Torsion

International Journal of Materials Research (formerly Zeitschrift fuer Metallkunde)

Vol. 100 (2009), pp. 1653-1661

[64] D. Geist, C. Rentenberger, H. P. Karnthaler

Extreme Structural Inhomogeneities in High-Pressure Torsion Samples along the Axial Direction

Acta Materialia

Vol. 59 (11) (2011), pp. 4578-4586

[65] R. B. Figueiredo, T. G. Langdon

Development of Structural Heterogeneities in a Magnesium Alloy Processed by High-Pressure Torsion.

Materials Science and Engineering: A

Vol. 528 (13) (2011), pp. 4500-4506

[66] R. B. Figueiredo, M. Kawasaki, T. G. Langdon

An Evaluation of Homogeneity and Heterogeneity in Metals Processed by High-Pressure Torsion

Acta Physica Polonica

Vol. 3 (2012), pp. 425-429

[67] R.B. Figueiredo, M. T. P. Aguilar, P. R. Cetlin, T. G. Langdon

Analysis of Plastic Flow During High-Pressure Torsion

Journal of Materials Science

Vol. 47 (22) (2012), pp. 7807-7814

[68] Y. Song, W. Wang, D. Gao, E. D. Yoon, D. J. Lee, H. S. Kim

Finite Element Analysis of the Effect of Friction in High-Pressure Torsion

Metals and Materials International

Vol. 20(3) (2014), pp. 445-450

[69] H.S. Kim, Y. Song, M. Chen, B. Xu, D. Gao, J. Guo, L. Xu, Z. Wang

Effects of Friction and Anvil Design on Plastic Deformation During the Compression Stage of High-Pressure Torsion

Korean Journal of Metals and Materials

Vol. 54 (11) (2016), pp. 831-837

[70] D. J. Lee, E. Y. Yoon, L. J. Park, H. S. Kim

The Dead Metal Zone in High-Pressure Torsion

Scripta Materialia

Vol. 67 (4) (2012), pp. 384-387

[71] Y. Cao, M. Kawasaki, Y. B. Wang, S. N. Alhajeri, X. Z. Liao, W. L. Zheng, S. P. Ringer, Y. T. Zhu & T. G. Langdon

Unusual Macroscopic Shearing Patterns Observed in Metals Processed by High-Pressure Torsion

Journal of Materials Science

Vol. 45 (17) (2010), pp. 4545-4553

[72] N. X. Zhang, M. Kawasaki, H. Ding, T. G. Langdon

An Examination of Microstructural Evolution and Homogeneity in a Magnesium AZ80 Alloy Processed by High-Pressure Torsion

Materiahrals Science and Engineering: A

Vol. 806 (2021), Article 140832

[73] N. Beckmann, P. A. Romero, D. Linsler, M. Dienwiebel, U. Stolz, M. Moseler, P. Gumbsch

Origins of Folding Instabilities on Polycrystalline Metal Surfaces

Physical Review Applied 2

Vol. 2 (6) (2014), pp. 1-7

[74] Wei, Jiang & Zhou, Hao & Cao, Yang & Nie, Jinfeng & Li, Yusheng & Zhao, Yonghao & Kawasaki, Megumi & Langdon, Terence & Zhu, Yuntian. (2019).

On the Heterogeneity of Local Shear Strain Induced by High‐Pressure Torsion

Advanced Engineering Materials

Vol. 22 (2019) Article 1900477

[75] R. Kulagin, Y. Beygelzimer, Y. Ivanisenko, A. Mazilkin, H. Hahn,

Modelling of High-Pressure Torsion using FEM. International Conference on the Technology of Plasticity

Procedia Engineering

Vol. 207(2017), pp.1445-1450

[76] R. Kulagin, Y. Beygelzimer, Y. Ivanisenko, A. Mazilkin, H. Hahn.

High-Pressure Torsion: from Laminar Flow to Turbulence

IOP Conference Series: Materials Science and Engineering, Materials Science and Engineering

Vol. 194 (2017) Article 012045

CRediT Authorship Contribution Statement

Dr Luis Vicente. Wilches Pena. Writing - original draft, visualization, methodology, investigation, formal analysis. **Prof Ling Wang.** Supervision, conceptualization, project administration, funding acquisition, writing - review & editing. **Prof Brian. G. Mellor.** Supervision, conceptualization, methodology, writing - review & editing. **Dr Yi Huang.** Methodology, investigation writing - review & editing.

Declaration of interests

☒ The authors declare that they have no known competing financial interests or personal relationships that could have appeared to influence the work reported in this paper.

☐The authors declare the following financial interests/personal relationships which may be considered as potential competing interests:

Highlights

- High – Pressure Torsion tests (HPT) to achieve Severe Plastic Deformation conditions (SPD) on annealed AISI 52100 bearing steel.
- HPT reproduces microstructures similar to the white etching areas (WEAs) observed on failed wind turbine bearings.
- LOM and SEM characterisation allows identification of two different white structure groups on HPT samples.
- Interruption of plastic flow on HPT samples are responsible to the white structure formation.